Journal of Power Sources 326 (2016) 93–103

Contents lists available at ScienceDirect

Journal of Power Sources

journal homepage: www.elsevier.com/locate/jpowsour

In operando neutron diffraction study of a commercial graphite/(Ni, Mn, Co) oxide-based multi-component lithium ion battery

N.S. Nazer [a, b], V.A. Yartys [a, b, *], T. Azib [c], M. Latroche [c], F. Cuevas [c], S. Forseth [d], P.J.S. Vie [a], R.V. Denys [a], M.H. Sørby [a], B.C. Hauback [a], L. Arnberg [b], P.F. Henry [e]

[a] *Institute for Energy Technology, Kjeller, Norway*
[b] *NTNU, Trondheim, Norway*
[c] *Université Paris Est, ICMPE (UMR7182), CNRS, UPEC, F-94320 Thiais, France*
[d] *FFI, Norway*
[e] *European Spallation Source ERIC, Sweden*

HIGHLIGHTS

- A 10,440 type commercial LIB was studied *in operando by* neutron diffraction.
- A three-phase mixture of $Li(Ni,Mn,Co)O_2$, $LiCoO_2$ and $LiMn_2O_4$ was identified as cathode.
- Graphite anode forms a series of insertion-type lithiated derivatives, including LiC18.
- On charging, a volume shrinkage is observed for the Li- depleted $Li0.2(Ni,Mn,Co)O_2$.
- $LiCoO_2$ has a lower capacity and expands when transforming into $Li0.4CoO_2$.

GRAPHICAL ABSTRACT

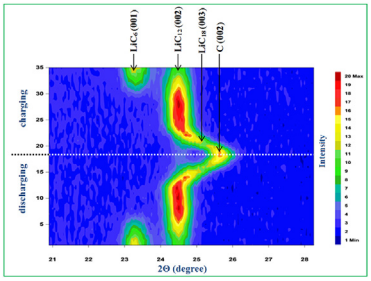

ARTICLE INFO

Article history:
Received 5 March 2016
Received in revised form
21 June 2016
Accepted 24 June 2016

Keywords:
Lithium ion battery
Layered oxides
In situ neutron powder diffraction
Graphite anode

ABSTRACT

In situ neutron diffraction was employed to investigate the structural evolution of the electrode materials in an ICR 10440 commercial cylindrical lithium-ion battery, which has a discharge capacity of 360 mAh and a nominal voltage of 3.7 V. A three-phase mixture of $Li(Ni,Mn,Co)O_2$, $LiCoO_2$ and $LiMn_2O_4$ was identified as the active material of the cathode, with graphite acting as the anode material. The study revealed that the graphite anode underwent structural changes to form a series of insertion-type lithiated derivatives, with up to 12.7% volume expansion for the Li-saturated compound LiC_6. The charge-discharge behavior was more complex for the cathode. Here, the charge process was associated with partial lithium depletion from the initially Li-saturated compounds, leading to volume shrinkage for $Li(Ni,Mn,Co)O_2$, in contrast to (Ni,Mn)-free $LiCoO_2$. Electrochemical discharge experiments performed under a fast regime (2 C) at 5, 25 and 45 °C revealed that the discharge capacity followed the trend of an increased diffusion rate of Li^+ ions in the electrolyte and Li atoms in both electrodes, being highest for 45 °C. At the lowest tested temperature (5 °C), a rapid drop in the discharge capacity took place using the same kinetic regime.

* Corresponding author. Institute for Energy Technology, Kjeller, Norway.
E-mail address: volodymyr.yartys@ife.no (V.A. Yartys).

http://dx.doi.org/10.1016/j.jpowsour.2016.06.105
0378-7753/

1. Introduction

Li-ion batteries (LIBs) provide high volumetric and gravimetric energy densities, in the range 250–450 Whl^{-1} and 100–210 $Whkg^{-1}$, well above the values for alternative rechargeable batteries [1]. Nevertheless, LIBs require improvements in their safety while also increasing their storage capacity, charge/discharge rates, and lifetime.

Although LIBs have many attractive features, a few key issues must be addressed to extend their practical applications, particularly towards their use in electric and hybrid electrical vehicles (HEVs), which require not only large energy storage capacity but also high rates of charge and discharge. Use at high and low operating temperatures and at high charge/discharge rates lowers charge/discharge efficiency, decreases the battery lifetime and can cause serious safety problems [2–4]. Therefore, heat control and management becomes an increasingly important issue for improving the reliability of the LIBs.

Rechargeable LIBs undergo structural transformations during charge-discharge cycles and, ultimately, face limitations in their lifetimes, due to irreversible capacity losses, voltage fade and even operational failures. LIBs operate by intercalation and deintercalation of lithium atoms into the anode and cathode, commonly described as a "rocking chair" mechanism, involving transport of Li^+ ions through the electrolyte and oxidation/reduction processes at the surface of the electrodes. During charge and discharge cycles, lithium ions are extracted from and reintercalated into the electrodes, in processes where non-stoichiometric compounds are formed [5]. In order to understand the processes affecting battery operation, it is necessary to probe the mechanism and kinetics of the phase-structural transformations in the cathode and anode as a function of testing conditions, such as charge-discharge current density, temperature and cycling history. This also includes the battery status during overcharge, when the thermal response of the battery is closely related to the cathode chemistry. When all Li is removed from the cathode, a rapid increase in heat generation can happen [6]. Overcharging removes more Li from the cathode than the lower limit of Li composition that allows reversible charge-discharge performance, leading to permanent structural changes and often happens at increased oxidation potentials.

Layered lithium cobalt oxide $LiCoO_2$ (LCO) is the predominant cathode material presently used in commercial lithium batteries, owing to its excellent cycle stability and low self-discharge. The drawbacks of LCO are the high price of cobalt, its relatively moderate specific discharge capacity (155 mAh/g) that is just half that of the graphite anode, and safety concerns caused by oxygen evolution and thermal runaway that can result in battery fires [7].

The isostructural lithium nickel oxide $LiNiO_2$ (LNO) has a higher reversible electrochemical capacity, forming $Li_{0.28}NiO_2$ at the highest state of discharge, which is 30% higher than $LiCoO_2$ [8]. Unfortunately, high lithium extraction leads to partial nickel substitution on the Li site, creating instabilities in the metal sublattice that negatively impact cycle life. Mixed composition $Li(Ni,Co)O_2$ and $Li(Ni,Mn,Co)O_2$ [9] are utilized to avoid the drawbacks for both Co (low capacity) and Ni (low cycle stability) layered oxides, while retaining the benefits from their strengths (favorable performance at high current densities and long calendar life for Co and high capacity for Ni layered oxides). Furthermore, partial substitution of Mn for Ni and Co prevents thermal instability in the layered oxides cathode, avoiding thermal runaway.

Various ratios of Ni, Mn and Co are selected and optimized to suit their applications as commercial electrodes. These include NMC 532 ($LiNi_{0.5}Mn_{0.3}Co_{0.2}O_2$), NMC 422 ($LiNi_{0.4}Mn_{0.2}Co_{0.2}O_2$) and NMC 622 ($LiNi_{0.6}Mn_{0.2}Co_{0.2}O_2$) in addition to the equiatomic composition $Li(Ni_{1/3}Mn_{1/3}Co_{1/3})O_2$, which displays the highest rechargeable capacity of 200 mAh/g. Optimization of the composition allows advanced electrochemical performance, combined with a high stability, better performance and low cost, to be achieved.

Another family of oxide-based cathode materials, based on the environmentally friendly, safe and less expensive $LiMn_2O_4$ [10], crystallizes with a spinel type. The discharge capacity of $LiMn_2O_4$ is rather low, not exceeding 120 mAh/g. However, its higher operating voltage of 4.1 V compared with LCO (3.9 V) and NMC oxides (3.8 V), together with rather high electric conductivity, beneficially affect the electrode and battery performance of composite mixtures of $LiMn_2O_4$ and layered oxides, particularly beneficial when applied in high power batteries.

Spinel type $LiMn_2O_4$ electrodes are more stable, both structurally and thermally, to Li extraction than Co and Ni based layered oxides [11]. $LiMn_2O_4$ and its chemically related layered oxide counterpart Li_2MnO_3, with higher Li content, together act as a reservoir for excess lithium that can diffuse from the transition metal layers into the adjacent lithium-depleted parts of the electrode during charging, stabilizing the electrode structure and enabling high practical capacities. This is caused by both the high diffusion coefficient of Li in Mn-based lithiated oxide and the presence of 3D Li + ion diffusion channels in spinel $LiMn_2O_4$, ensuring excellent rate performance at high charge-discharge densities [12]. An extra feature of $LiMnO_4$ is in its structural compatibility with the close packed oxygen array in the layered oxide structures making the spinel material an ideal candidate for integration into composite systems.

Integration of spinel $LiMn_2O_4$ [13] stabilizes the capacity and voltage of Co and Ni based layered oxides. $LiMn_2O_4$ enables LCO domains to sustain an upper cut-off voltage as high as 4.8 V without experiencing irreversible structural changes. At high applied voltage, problems arising from irreversible structural phase transitions are typical challenges in utilizing many of the layered oxides. Compositional tuning, surface coatings and metal doping are possible ways of dealing with structural degradation [14]. The available reference data show that integration of various materials into a composite cathode allows retention of the properties of the individual components and is a suitable pathway to build advanced cathode electrodes that are superior to the constituent single phase analogues.

The LIBs battery probed in the present study contain a mixture of the layered oxides, $Li(Ni,Mn,Co)O_2$, $LiCoO_2$ and $LiMn_2O_4$ in the cathode and graphite as the anode material. Layered transition-metal oxides of the $Li(Ni,Mn,Co)O_2$ family belong to the most popular cathode materials for the high voltage LIBs, where a two-dimensional Li^+ ion diffusion takes place. In turn, natural graphite is a standard, presently commercially used anode material, with a high theoretical discharge capacity of 372 mAh/g. Intercalation and deintercalation processes of lithium into/from graphite are well understood, with several staged phase transformations identified as:

Stage 1. (C) ↔ Li_xC_{12}; **Stage 2.** Li_xC_{12} ↔ LiC_{12}; **Stage 3.** LiC_{12} ↔ LiC_6[15].

As a cathode of the LIBs, LCO is often used due to its high capacity (200 mAh/g) and good cyclability. A recent trend by the battery manufacturers is utilizing a mixed nickel-manganese-cobalt $Li(Ni,Mn,Co)O_2$ oxide, not only due to its high discharge capacity of 280 mAh/g, but mostly because of a combination of strengths characteristic for the individual lithiated oxides formed by cobalt, nickel or manganese. The nickel layered oxide is known for its high specific energy but poor stability and manganese brings the benefit of forming a spinel type structure to achieve a good electric conductivity and low internal resistance but suffers from a

low specific energy.

Neutron scattering allows *in operando* monitoring of the various processes and properties involved upon cycling, due to the deep penetration depth of neutrons into solid-state materials. A3 type rechargeable batteries (diameter 10 mm; length 45 mm), which are studied in the current work, are well matched with the experimental layout of neutron scattering beamlines, for example SINQ neutron source at Paul Scherrer Institute, Switzerland. The high neutron flux allows study of processes on a relatively short time scale. In the present study, neutron diffraction data sets were accumulated, with a quality sufficient for full Rietveld refinement, in just 3–5 min. Importantly, neutron powder diffraction is sensitive to the light element lithium in the presence of heavier elements and can also be used to distinguish the neighbouring transition metals – Mn, Fe, Co and Ni – thus overcoming inherent limitations of X-ray diffraction technique [16]. These properties are ideal to probe atomic positions of the species within each phase as well as phase evolution.

Various aspects of *in situ* studies of Li ion batteries, based on the use of synchrotron XRD, conventional XRD and NPD, including design of the *in situ* cells, development of the electrode materials and comparison of different *in operando* techniques, were recently reviewed in Ref. [17]. *In operando* and *in situ* studies reveal the evolution of the reactions occurring including probing formation of intermediate phases, as well as yielding crystallographic data of the phases present and their transformations at different applied voltages and currents.

The vast majority of the reference works [18–26] on *in situ* NPD characterization of commercial battery performances focused on studies of the 18650 LIB (18.6 mm diameter x 65.2 mm length), measuring discharge capacity between 1950 and 2600 mAh). This cell type is used in Tesla electric vehicles, laptop batteries and LED flashlights. Table 1 presents a summary of the data reported in the reference works and includes the papers published in 2010–2015.

All commercial 18650 batteries studied used graphite as the anode, while the cathode materials utilized three different types of layered oxides. These included NMC oxide with two different stoichiometries, an equiatomic $LiNi_{1/3}Co_{1/3}Mn_{1/3}O_2$ oxide [18,19], a 532 type $LiNi_{0.5}Mn_{0.3}Co_{0.2}O_2$ oxide [20] and $LiCoO_2$ [21–26].

Variable test temperatures and charge-discharge rates were exploited. The most common case was maintaining the battery at ambient conditions (though subzero test conditions (−20 and −38 °C) and elevated temperature of 50 °C, were also applied), while the current densities used varied between 0.01 C and 1 C.

The voltage window applied during charge-discharge most frequently spanned the safest recommended by the battery producers range of operation conditions - between 3.0 and 4.2 (3.0–4.2 V). However, overcharge up to 4.6 V and over-discharge to 2.0 V were also probed to investigate testing voltage and possible degradation of the battery.

The mechanisms of the charge–discharge processes were described in the reference data in detail for both cathode and anode. The findings made in the literature can be summarized as follows:

1.1. Cathode

The highest lithium content reached during discharge was 0.95 at.Li/f.u. $LiTMO_2$ (TM = transition metal: Ni, Co, Mn) [22]. The change of lithium content during the charge was associated with a modulation of the unit cell parameters of the trigonal unit cells, which underwent modifications, first a continuous increase of the *c* lattice parameter before reaching maxima, with a follow-up decrease of *c* at the latest stages of the process. In contrast, the *a* lattice parameter decreased monotonically during the charge [20]. Cycling resulted in decreased discharge capacities, caused by narrowing of the window for the reversible change in Li content between the saturated and depleted Li oxides, so the first became smaller while the second increased [18]. Investigations of current density-dependent fluctuations of lattice dimensions showed that, at higher currents, an increase in the *c* unit cell parameter of the charged cathode was smaller than that observed for the lower currents. Cation mixing between Li ion and transition metals (Ni,Mn,Co) in the NMC lattice was observed, with Li occupying the 3*b* sites in addition to the regular 3*a* sites [20]. A continuous phase transition within a single phase region was observed for the NMC oxide, while $LiCoO_2$ exhibited a phase separation with formation of a (small) two-phase region during the charging [19,26]. During the cycling of the $LiCoO_2$ cathode containing a mixture of the layered oxide and a spinel oxide, similar changes in lithium content in these phases were observed during the charge/discharge process.

1.2. Anode

Formation of the lithium intercalated derivatives LiC_6 (maximum Li content) and LiC_{12} were reported in all studies. At low lithium content, a number of Li-based intercalates (Li_xC_{54}, Li_xC_{18}, Li_xC_{24} …) were obtained and characterized [18]. The mechanism of their formation-decomposition was dependent upon the testing

Table 1
Data presented in the reference papers on the *in situ* neutron diffraction studies of commercial LIB using layered oxides as cathode material.

Type of cell	Cell capacity (mAh)	Type of cathode	Voltage range (V)	Temperature (°C)	Regime of discharge/ charge	Transformations in anode	Transformations in cathode
18650 [18]	1950	NMC1	3–4.2	−20	0.2C/0.033C	Li_xC_{54}, Li_xC_{18}	***
18650 [19]	2250	NMC1	3–4.5	22.5	0.2C	LiC_{18}	***
18650 [20]	2200	NMC2	3–4.2	RT	0.18C	*	$Li_{0.26}$ (NMC)O_2
18650 [21]	2600	$LiCoO_2$	3–4.2	RT	0.058C/0.029C	*	***
18650 [22]	2600	$LiCoO_2$	3–4.2	25/50	1C/0.15C	*	$Li_{0.5/0.39}CoO_2$
18650 [23]	2500	$LiCoO_2$	2.5–4.2	22.5	0.5C/−0.2C,0.8C	LiC_{18}	***
18650 [24]	2600	$LiCoO_2$	3–4.2	26/46/−3/−23/−33/-38/−43	0.01C	*	***
18650 [25]	2000	$LiCoO_2$	3–4.2	RT	1C	*	$Li_{0.82/0.77}CoO_2$ (3.4 V,fresh/ 3.6 V,fatigue) −$Li_{0.17/0.09}$ (4.2 V,fresh/4.2 V fatigue)
18650 [26]	2500	$LiCoO_2$	2–4.6	RT	0.6C	LiC_{18}	***
Pouch cell [27]	40000	NMC-$Li_xNi_yMn_zCo_{(1-y-z)}$	2.7–4.2	RT	0.8C	LiC_{24}	***

NMC1 = $LiNi_{1/3}Co_{1/3}Mn_{1/3}O_2$; NMC2 = $LiNi_{0.5}Mn_{0.3}Co_{0.2}O_2$.
* C ↔ LiC_{12} ↔ LiC_6 was reported in all reference data. ** Data is missing. ***Not studied in detail.

conditions (current density, temperature, cycling) and different types of Li ordering were observed. The *in situ* studies revealed that the mechanism of transformations in the Li–C system is temperature-dependent and that the ordered lithiated intercalates do not form at subzero temperatures, where LiC_{12} directly transforms into the graphite. At high lithium content in the Li intercalates, the extent of completeness of the process of lithiation $LiC_{12} \rightarrow LiC_6$ was dependent upon the voltage applied [24]. At 4.2 V, which is the highest recommended charge voltage for the LIB, LiC_{12} and LiC_6 co-exist. However, when an overcharge potential of 4.6 V is applied, all LiC_{12} was converted to LiC_6 [25].

A new electrochemical cell for the *in situ* NPD study of the electrode materials was reported in Refs. [28], where the cell was made from a null matrix Ti–Zr alloy, thus assuring collection of a high quality NPD data. The neutron beam irradiated only the bottom part of the cell where the powdered cathode electrode materials ($LiFePO_4$ or $Li_{1.1}Mn_{1.9}O_4$) were located.

The objective of this work was to provide a full structural characterization by *in operando* neutron diffraction of a commercial Li-ion battery containing a composite multicomponent cathode and a graphite anode. The aim was to study and characterize the individual behaviors and performances of the various components of the electrodes in order to establish their synergies.

The work performed was different from the earlier studies of the LIBs in three important aspects.

First, the cathode was not a single phase material as in all earlier works, but contained three electrochemically active constituents, with $LiCoO_2$ and a 532 NMC oxide as majority phases and spinel type $LiMn_2O_4$ as minority phase. Secondly, the battery type was ICR 10440 (diameter 10 mm, length 40 mm; discharge capacity 360 mAh, nominal voltage 3.7 V), which was not probed in any other published report. The battery capacity is 5–6 times lower than in the reference works, with a diameter nearly half that of the reference data. This gives a better chance to avoid space inhomogeneities during *in operando* battery tests, thus allowing characterization at conditions closer to thermodynamic equilibrium. Finally, low rates of charge and discharge were utilized, C/12.5, to achieve better equilibrium in the battery electrodes.

NMC cathodes show better stability during the cycling, even at elevated temperatures, and have a higher reversible capacity when compared with the $LiCoO_2$ cathode. Upon Li extraction/insertion, the structure of the NMC and $LiCoO_2$ cathodes distort, leading to changes in the unit cell volumes. While NMC and $LiCoO_2$ were studied separately in the reference works, their parallel evolution when a competitive redistribution of lithium is allowed has not been previously studied. A possible difference in the evolution of the cathode materials during de/intercalation made our work more challenging during analysis.

2. Experimental

A commercial cylindrical battery ICR 10440 (diameter 10 mm, length 40 mm, discharge capacity 360 mAh, nominal voltage 3.7 V), which was manufactured by Great Power Battery Co., Ltd. (H.K./China), was used. Its electrochemical performance was tested by galvanostatic cycling at temperatures from 5 to 45 °C and kinetic regimes from 0.1 to 2C (where C/*n* denotes the rate at which a full charge of the battery takes *n* hours). The morphology of the electrodes as well as the composition and crystal structure of the containing phases were analyzed for the as delivered battery prior to the neutron diffraction measurements. For this purpose, the battery was disassembled in a glove box and the electrodes were rinsed with dimethycarbonate (DMC). Morphological and chemical studies were performed using a Hitachi SU6600 scanning electron microscope with energy dispersive X-ray spectroscopy (SEM/EDAX). Structural analysis by X-ray Diffraction (XRD) was conducted with a D8-Bruker diffractometer (Bragg-Brentano geometry, Cu-K_α radiation) equipped with a graphite rear-monochromator. The electrodes were protected with a Kapton foil to avoid oxidation in air.

The neutron diffraction experiments were conducted using HRPT [29] diffractometer, at Paul Scherrer Institute, using a wavelength of $\lambda = 1.494$ Å. The experimental setup for the diffraction measurements is shown in Supplementary Information, Fig. S1.

Before the neutron experiments the as-received battery went through a discharge-charge galvanostatic cycle at the Institute for Energy Technology (IFE). The battery used in the NPD experiments was charged to reach a cut-off voltage of 4.2 V, showing a charge capacity of 345 mAh. Subsequently, the battery was discharged and charged *in situ* at PSI in a potential window 3.0–4.2 V, galvanostatic mode, using a portable SP50 potentiostat from BioLogic. The kinetic regimes were fixed at C/12.5 with discharge/charge half-cycles accomplished in 12.5 h. The NPD pattern under fully charged and discharged conditions were measured for 0.6 h. Rietveld refinements of the diffraction patterns were carried out using the GSAS suite of program with the EXPGUI interface [30,31].

2.1. Characterization of the battery electrodes

2.1.1. Characterization of the cathode material

2.1.1.1. X-ray diffraction study. The phase and structural composition of the active material of the cathode was studied by XRD. The diffraction pattern is given in Fig. 1.

Indexing of the pattern showed that the sample contained two Li-containing "layered oxide" type phases, crystallizing with the α-$NaFeO_2$ type of trigonal crystal structure (space group $R\bar{3}\ m$). The values of the unit cell parameters were refined using GSAS to be:

Phase 1: $a = 2.8120(1)$ Å; $c = 14.226(1)$ Å; $V = 97.419(5)$ Å^3;

Phase 2: $a = 2.8276(1)$ Å; $c = 14.494(1)$ Å; $V = 100.357(8)$ Å^3.

In addition, one extra, minority oxide phase with a spinel type crystal structure and unit cell parameter of the FCC unit cell of $a = 8.220$ (2) Å; $V = 555.4(5)$ Å^3, was identified.

The two layered oxides have similar unit cell parameters but the small, yet significant, difference in the values of the values of *a* and *c* result in splitting of the diffraction peaks with the same Bragg indexes. Some characteristic XRD peaks and their splitting are

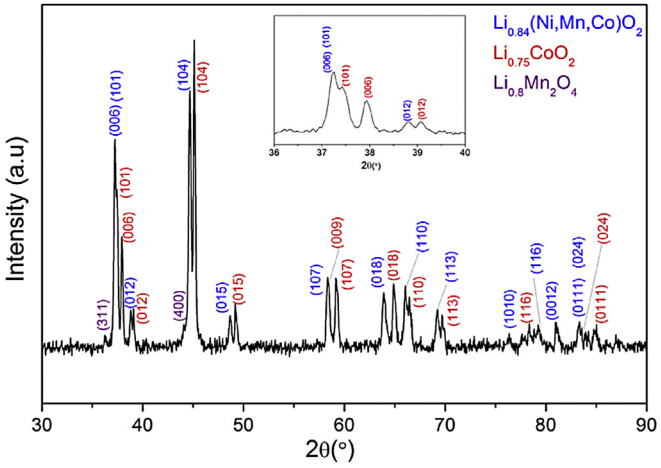

Fig. 1. XRD pattern of the cathode material. The inset shows the splitting of the (101) and (102) peaks.

illustrated in Fig. 1.

Elemental analysis showed that three transition metals *(TM)*, Ni, Co and Mn, contribute to the composition of the layered oxides. One layered oxide was identified as Li_xCoO_2 (phase 1; see Fig. 3 and the following subsection), while the second oxide phase was found to contain all three *TM*s with a composition $Li_x(Ni,Mn,Co)O_2$ (phase 2, $Li(Ni_{0.52}Mn_{0.24}Co_{0.24})O_2$).

In the α-$NaFeO_2$ structure type (Ni,Mn,Co) and Li atoms form alternating planes, which stack in an ABCABC sequence filling the interstices of the oxygen anion framework. This structure contains Li-ions in the 3*a*, the transition metal ions (Ni,Mn,Co) in 3*b* and O ions in the 6*c* sites (space group $R\bar{3}\,m$; see Fig. S2).

For the layered oxide structures, the occupancy on the Li site can vary between complete filling and a partial occupancy. In the as-delivered battery, the values of the unit cell parameters for phase 1 agree well with the reference data for the Co-based $Li_{0.75}CoO_2$ (a = 2.823 Å; c = 14.22 Å) [32] with a 75% occupancy on the Li site. In turn, a comparison with the reference data shows that the unit cell parameters for phase 2, NMC oxide, are rather close to the reference data for the 532 oxide with a composition $Li_{0.84}(Ni_{0.5}Mn_{0.3}Co_{0.2})O_2$ (a = 2.829 Å, c = 14.495 Å) [33]. The measured EDS chemical composition for phase 2, $Li_x(Ni_{0.52}Mn_{0.24}Co_{0.24})O_2$, is also very similar to the reference values.

The minority oxide was identified as the Mn-based spinel $LiMn_2O_4$, and showed a good agreement of the unit cell parameter with the value of a = 8.220 Å reported in Ref. [34] for $Li_{0.8}Mn_2O_4$, with 80% occupancy on the Li site.

2.1.1.2. Morphology of the cathode material. The morphology and composition of the active cathode material deposited on the aluminum current collector were characterized by SEM and EDS. As mentioned earlier, the active material consists of three oxide phases formed by three different *TM*s (Ni, Mn and Co). The micrograph in Fig. 2 (see also Fig. S3) shows the elemental distribution maps of the *TM*s. These exhibited spatial inhomogeneities indicating the presence of the phase constituents enriched by Ni-, Co- and Mn-rich oxides, displayed as green, red and blue colored regions respectively. The relative amount was estimated from the respective area in the micrograph as 48 (Ni-rich NMC), 47 (LCO), 5 ($LiMn_2O_4$) %.

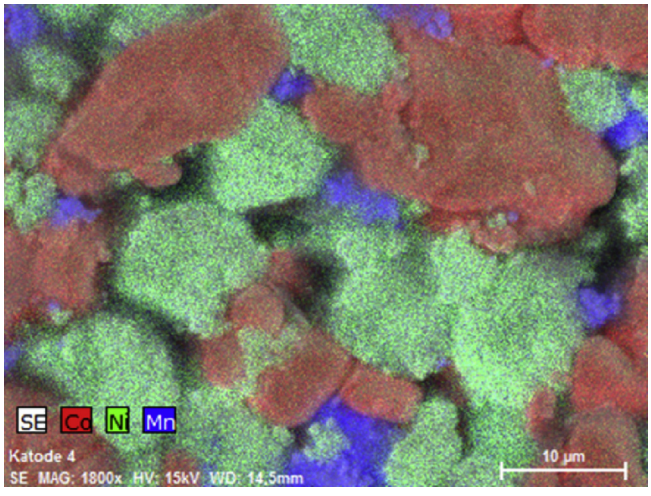

Fig. 2. Elemental X-ray mapping from SEM/EDS analysis (Ni in green, Co in red, Mn in blue) of the cathode material containing three oxide phases: Phase 1, $LiCoO_2$ (red); Phase 2, 532 type $Li(Ni,Mn,Co)O_2$ oxide (green), and $LiMn_2O_4$ (blue). (For interpretation of the references to color in this figure legend, the reader is referred to the web version of this article.)

The EDS analysis of the *TM*s in the Ni-rich oxide was 52:25:23 wt% Ni:Mn:Co. In combination with the data of the XRD analysis (see below), a composition of the NMC layered oxide was calculated as $LiNi_{0.52}Mn_{0.24}Co_{0.24}O_2$. The Co-rich and Mn-rich oxides each contained a single *TM*. Their compositions were determined to be $LiCoO_2$ and $LiMn_2O_4$, respectively, from the EDS and XRD analysis.

The three regions exhibited different morphologies. The Co region (Phase 1) consisted of dense particles, between 5 and 10 μm in size, while the Ni-rich phase (Phase 2) was characterized by an assembly of fine particles (<1 μm) agglomerated into larger domains about 10 μm in size. The Mn-based phase displayed an intermediate particle size of 3–8 μm.

2.1.2. Characterization of the anode material

The morphology and composition of the active material deposited over the negative current collector were characterized by SEM-EDS (Fig. 3). Morphological characterization confirmed a uniform deposit with cracks and porosity. The major constituent was found to be carbon; EDS analysis yielded C (71.6 wt %), and O (26.4 wt %) and minor impurities such as F (1.6 wt %) and P (0.4 wt %). The average size of the particles was 10 μm. Presence of oxygen was attributed to a short exposure of the electrode to the atmosphere during its transfer to the SEM chamber. Fluorine and phosphorus are residues from the electrolyte salt, $LiPF_6$.

Two phase constituents were identified from the XRD analysis of the anode electrode (see Fig. S4): lithiated graphite LiC_{12}, together with metallic Cu (current collector; sp.gr. $Fm\bar{3}m$; a = 3.6159 Å). Diffraction peaks from the LiC_{12} phase were indexed in the P6/*mmm* space group with the unit cell parameters a = 4.288 Å and c = 7.063 Å. The observed values of a and c are in excellent agreement with the reference data, a = 4.287 Å, c = 7.066 Å [35].

2.2. Electrochemical measurements

Influence of applied current density on the discharge capacity at different temperatures

The battery was electrochemically cycled in a galvanostatic mode with applied currents (kinetic regimes) of 0.035 A (0.1C), 0.07 A (0.2C), 0.17 A (0.5C), 0.35 A (1C), 0.75 A (2C) in the voltage window 4.2 - 3 V at three different temperatures (5, 25 and 45 °C). At applied testing conditions, the battery showed discharge capacities in the range 153–340 mAh illustrated in Fig. 4.

The capacity of the battery decreased in all cases with increase of the charge-discharge rates. The discharge voltage profiles at low C rates, 0.2 C and 0.5 C, displayed several plateaus at all temperatures, a feature characteristic of the layered oxide cathodes.

For the cell tested at room temperature, the specific discharge capacity of the cell at 0.1 C rate was 324 mAh and at 2 C it decreased to 288 mAh.

The battery discharge capacity reached the highest value at 45 °C (339 mAh), where it delivered 94% of its rated capacity. We assume that such a superior performance is due to the enhanced electrochemical kinetics and increased diffusion coefficient of Li^+/mass transport of Li in the electrodes at this temperature.

The cell discharge voltage profiles revealed a very interesting temperature-dependent behavior at high applied current densities. As the temperature decreases, the discharge capacity at high current dropped steeply. The observed capacity loss at low temperature may be due to the limitations imposed by a slower Li diffusion [36,37]. At 2 C rate and 5 °C, the discharge capacity dropped and did not exceed a half of its initial capacity, with a discharge curve developing a kink after surpassing the discharge capacity of 20 mAh. The development of the kink at 3.4 V probably resulted from temperature changes. The temperature at this point dropped

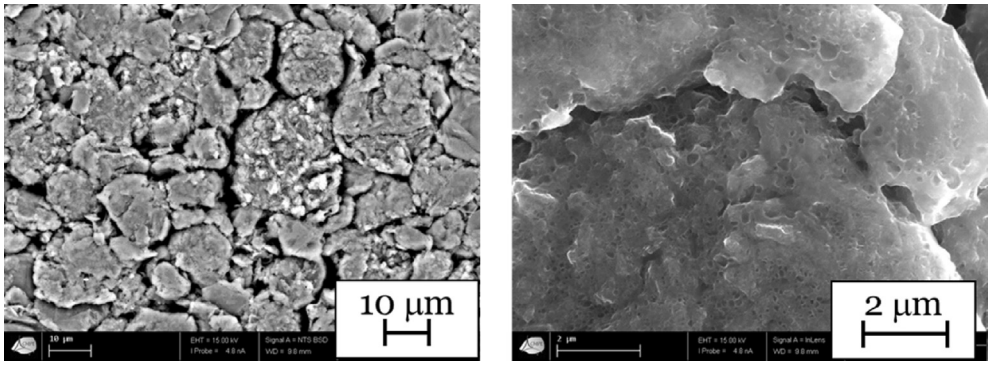

Fig. 3. SEM images of the graphite anode.

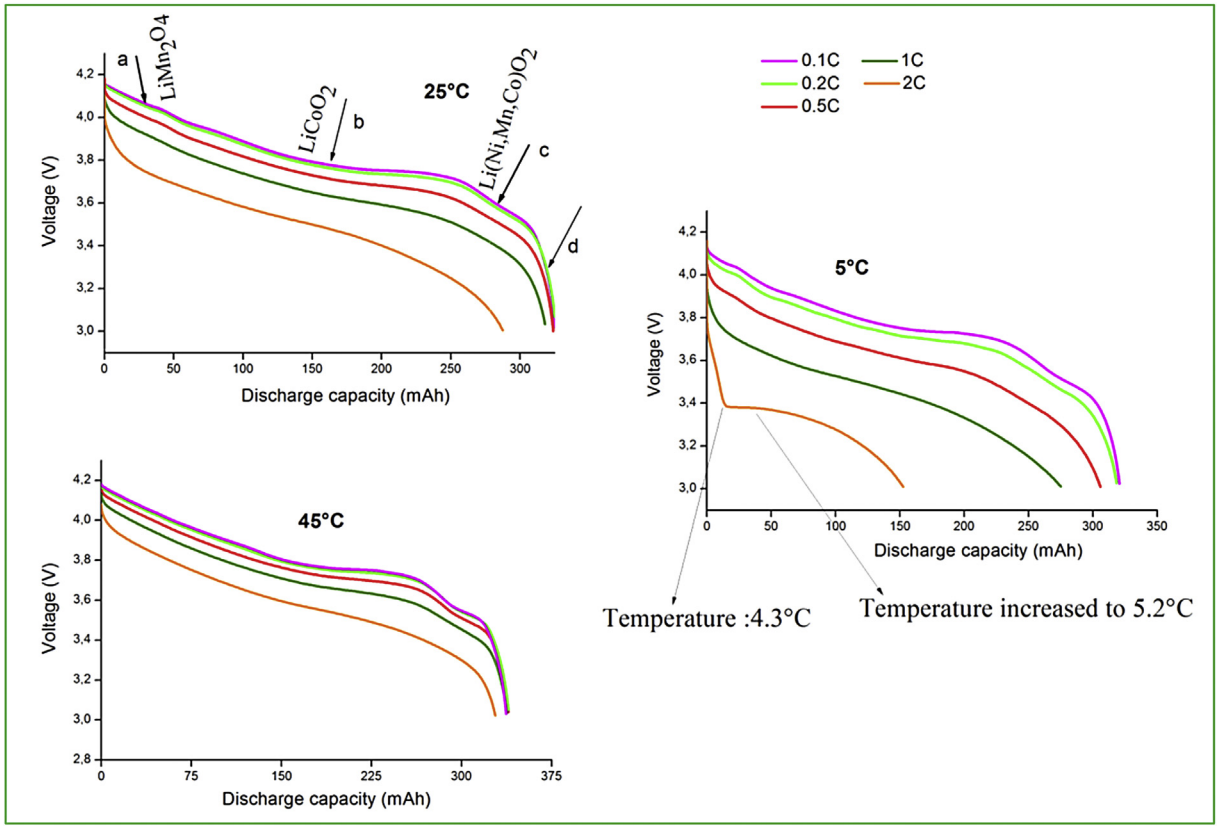

Fig. 4. Voltage profiles of the battery at 5 °C, 25 °C and 45 °C. The voltage plateaus (a) at 4.05 V, (b) at 3.97 V and (c) at 3.6 V are observed at the values well agreeing with the redox potentials of $LiMn_2O_4$, $LiCoO_2$ and $Li(NMC)O_2$, respectively.

below the setpoint value of 5 °C. However, after surpassing the discharge capacity of 20 mAh, the battery warmed up, because of the exothermic discharge process taking place, and therefore the discharge curve significantly flattened.

From Fig. 4 it is clear that at lower discharge current densities, voltage plateaus are observed at all temperatures. The voltage plateau region (b) starting at 3.97 V is related to the delithiation of $LiCoO_2$.The voltage plateaus (a) at 4.05 V and (c) at 3.6 V are associated with $LiMn_2O_4$ and the mixed oxide $Li(Ni,Mn,Co)O_2$, respectively. The end-of-discharge step (d), where a rapid drop of the potential takes place, is conventional for the battery behavior.

The discharge profiles of NMC, $LiCoO_2$ and $LiMn_2O_4$ at a rate of 0.1 C, are presented in Fig. 5 based on the reference data [38–40] and present further details of the cathode performances. The potential profile of $LiCoO_2$ shows a sloping voltage plateau spanning the range 4.2 to 3.5 V. The spinel $LiMn_2O_4$ has a double plateau discharge behavior in the potential range 4.3–2.5 V *vs.* Li/Li+, which indicates occurrence of a two-stage reversible intercalation/deintercalation process of lithium. The voltage plateau of NMC is 1.8 times steeper than that for $LiCoO_2$. Indeed, for the $LiCoO_2$, the slope $\Delta V/\Delta C$ is −0.0032 and for the NMC the slope $\Delta V/\Delta C$ is steeper, −0.0057. The voltage plateau for $LiNi_{0.5}Mn_{0.3}Co_{0.2}O_2$ is around 3.6 V. The steepness $\Delta V/\Delta C$ for this composition characterized from the reference data, 0.0057, while from our data the measured steepness in the region 3.9 V–3.75 V is equal to 0.0018.

Even though NMC and $LiCoO_2$ have the same type of the layered oxide structure, their reversible electrochemical capacity is different. Only 0.61 at. Li/f.u. can be reversibly electrochemically

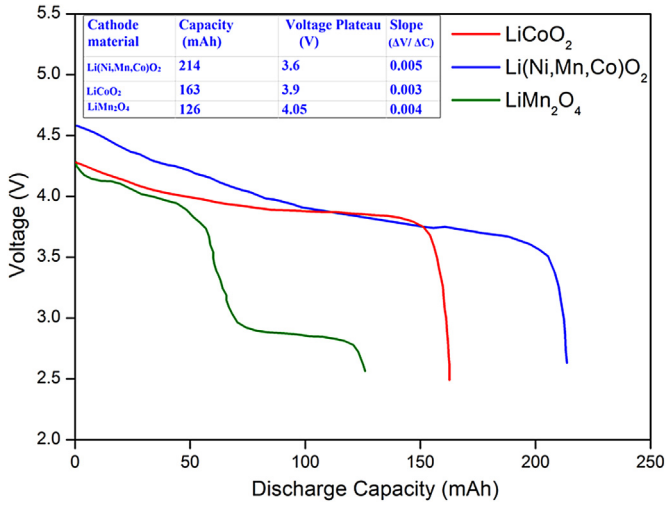

Fig. 5. Discharge profiles of the layered oxides $LiCoO_2$, $Li(Ni,Mn,Co)O_2$, and spinel $LiMn_2O_4$ at 0.1 C rate and at room temperature [38–40].

extracted from $LiCoO_2$ yielding $Li_{0.39}CoO_2$ [41]. In contrast, a larger amount of lithium, up to 0.74 Li, can be reversibly deintercalated from NMC [19], which forms $Li_{0.26}(NMC)O_2$ thus resulting in a higher capacity as compared to $LiCoO_2$. The reason for the observed differences is in the fact that manganese in $Li(Ni,Mn,Co)O_2$ is present in a +4 oxidation state, which allows the nickel atoms to remain in their stable +2 oxidation state This allows varying the content of Li in a broader range without affecting the thermodynamic stability of the lattice of the used NMC oxide.

From Fig. 4 (see also Fig. S5) it is obvious that the discharge capacity steeply decreases at the lowest used temperature of 5 °C. In contrast, at 45 °C, a stable performance of the battery is observed, with no significant decrease in the discharge capacity even at the highest current density of 2 C. The capacity drop at high current densities is more pronounced at room temperature as compared to the highest test temperature of 45 °C.

2.3. Neutron diffraction study of a fully charged and discharged battery

In order to understand the structural changes in the constituent electrodes, the neutron diffraction patterns were first collected at the fully charged and fully discharged conditions. The crystallographic characteristics of the phases present in the battery at the end-of-charge (EOC) and end-of-discharge (EOD) conditions are given in Table 2. Refined structural parameters are listed in Table 3.

Clear diffraction peaks (Fig. S6) from the cathode materials, copper and aluminium current collectors, iron casing as well as from graphite anode and lithium intercalated graphite derivatives were observed.

For the fully discharged battery, besides diffraction peaks from the $Li(NMC)O_2$ and $LiCoO_2$ cathode materials, we observed contributions from the graphite anode (C) and from LiC_{12}. Presence of LiC_{12} in the diffraction pattern indicates that the delithiation of the anode was incomplete. In the fully charged battery, two lithiated graphite derivatives, LiC_{12} and LiC_6, co-exist and are observed with nearly the same abundancies. Therefore, the graphite is not completely lithiated at this stage. Both discharge and charge observations reveal that the capacity of the anode was over-dimensioned as compared with that of the cathode by approximately 20%; *i.e.* that the mass of graphite in the anode is roughly 20% more than needed for complete rocking of Li between anode and cathode electrodes.

As mentioned earlier, the main components of the cathode electrode, $Li(Ni,Mn,Co)O_2$ and $LiCoO_2$ layered oxides, crystallize in the trigonal unit cells (space group $R\bar{3}\,m$, α-$NaFeO_2$ type phase). The refinements of the NPD pattern show that $R\bar{3}\,m$ symmetry and type of the structure are maintained throughout the charge-discharge. However, the charge-discharge affects the values of the unit cell parameters and occupancies of the Li sites. As a starting point of the refinements of the lattice parameters of the anode and cathode phases during the refinements of the NPD data, we have used the data from XRD refinements of the data measured for the as delivered battery (see earlier in the paper).

Analysis of the NPD refinements allowed us to suggest the electrochemical transformations taking place during the charge and discharge of cathode and anode:

2.3.1. Anode

The lithiation/delithiation of the graphite anode leads to the formation of a number of Li- intercalated graphite derivatives:

$$C + xLi^+ + xe^- \xleftrightarrow{\text{charge-discharge}} LiC_x \quad (x = 6,\ 12,\ 18)$$

Table 2
Crystallographic characteristics of the constituent phases at the end-of-charge (EOC) and at the end-of-discharge (EOD) obtained from Rietveld refinement of neutron powder diffraction data.

Phase	Space group	Unit cell parameters(Å)	EOC Phase abundance (wt.%)	EOD Phase abundance (wt.%)
[a]$Li(NMC)O_2$	$R\bar{3}\,m$	$a = 2.844(1)$ $c = 14.41(1)$	–	30(1)
[a]$Li_{0.2}(NMC)O_2$	$R\bar{3}\,m$	$a = 2.8182(8)$ $c = 14.467(5)$	26(2)	–
$LiCoO_2$	$R\bar{3}\,m$	$a = 2.817(3)$ $c = 14.060(2)$	–	31(1)
$Li_{0.4}CoO_2$	$R\bar{3}\,m$	$a = 2.8100(3)$ $c = 14.445(3)$	30(2)	–
C (graphite)	$P6_3/mmc$	$a = 2.4620(1)$ $c = 6.7266(8)$	–	31.1(3)
LiC_{12}	$P6/mmm$	$a = 4.2905(7)$ $c = 7.047(1)$	17.3(3)	7.9(5)
LiC_6	$P6/mmm$	$a = 4.3154(4)$ $c = 3.702(6)$	26.7(3)	–

[a] The ratio Ni:Mn:Co in the NMC phase was taken from the SEM-EDS data as 52:25:23 wt%. This data combined with XRD concluded that the composition of the NMC oxide is $Li(Ni_{0.5}Mn_{0.3}Co_{0.2})O_2$; this composition was used as an input into the NPD refinements. $LiMn_2O_4$ was not included into the NPD refinements as its amount is very low and its contribution to the neutron diffraction pattern is marginal.

Table 3
Crystal structure data for the present phases.

Phase	Space group, types of sites and atomic coordinates	Occupancy
[a]Li(Ni,Mn,Co)O_2	$R\bar{3}m$	
	Li in 3*a* (0, 0, 0)	1
	M in 3*b* (0, 0, ½)	1
	O in 6*c* (0, 0, 0.2614)	1
$Li_{0.2}$(Ni,Mn,Co)O_2	$R\bar{3}$ *m*	
	Li in 3*a* (0, 0, 0)	0.2
	M in 3*b* (0, 0, ½)	1
	O in 6*c* (0, 0, 0.2614)	1
$LiCoO_2$	$R\bar{3}$ *m*	
	Li in 3*b* (0, 0, 0)	1
	Co in 3*a* (0, 0, ½)	1
	O in 6*c* (0, 0, 0.2396)	1
$Li_{0.4}CoO_2$	$R\bar{3}$ *m*	
	Li in 3*b* (0, 0, 0)	0.4
	Co in 3*a* (0, 0, ½)	1
	O in 6*c* (0, 0, 0.2396)	1
Graphite	$P6_3/mmc$	
	C in 2*b* (0, 0, ¼)	1
	C in 2*c* ($^1/_3$, $^2/_3$, ¼)	1
LiC_{18}	*P*6/*mmm*	
	Li in1*a* (0, 0, 0)	1
	C in 6*k* (0.3333, 0, ½)	1
	C in 12*n* (0.3333, 0, 0.1667)	1
LiC_{12}	*P*6/*mmm*	
	Li in 1*a* (0, 0, 0)	1
	C in 12*n* (0.3333, 0, 0.25)	1
LiC_6	*P*6/*mmm*	
	Li in 1*a* (0, 0, 0)	1
	C in 6*k* (0.3333, 0, ½)	1

The U_{iso} were fixed to 0.01*100 Å^2 for atoms/phases and were not refined.
Li occupancies were fixed to the value obtained by comparing the lattice parameters with the reference data and were not refined. Positional parameter for O ($z = 0.2396$ ($LiCoO_2$), z = 0.2392 (NMC)) was taken from Refs. [32,19] and was not refined.
[a] For the NMC phase, M = Ni + Mn + Co with the atomic ratio 0.5:0.3:0.2 was used in the refinements.

2.3.2. Cathode

During the charging of the battery, the delithiation of the layered cathode materials takes place, until a certain limiting level of depletion of the layered oxide lattice by lithium takes place to form a related layered oxide structure with a lower content of Li.

The delithiation/lithiation is a single step process for $LiCoO_2$ and Li(Ni,Mn,Co)O_2:

$$LiCoO_2 \xleftrightarrow{\text{discharge-charge}} Li_{1-x}\,CoO_2 + xLi^+ + xe^- \quad (x = 0 - 0.6)$$

$$Li(Ni, Mn, Co)O_2 \xleftrightarrow{\text{discharge-charge}} Li_{1-x}(Ni, Mn, Co)O_2 + xLi^+ + xe^- \quad (x = 0 - 0.8)$$

In contrast, for $LiMn_2O_4$, the Li ion extraction/insertion is a two-step process, as shown in Fig. 5.

Step 1

$$LiMn_2O_4 \xleftrightarrow{\text{discharge-charge}} Li_{1-x}\,Mn_2O_4 + \ xLi^+ + xe^- (x = 0 - 0.5)$$

Step 2

$$Li_{1-x}\,Mn_2O_4 \xleftrightarrow{\text{discharge-charge}} Mn_2O_4 + (1-x)Li^+ + (1-x)e^- (x = 0.5 - 0.8)$$

Both for 532 NMC oxide and for $LiCoO_2$, the charge of the battery is associated with a delithiation process resulting in the formation of Li-poor derivatives $Li_{1-x}CoO_2$ and Li_{1-x}(NMC)O_2. For the Co-based oxide, the refined lattice parameters at the end of charge are $a = 2.8100(3)$ and $c = 14.445(3)$ Å. They are in good agreement with those reported for $Li_{0.4}CoO_2$ compound: $a = 2.80886(3)$ and $c = 14.4457(3)$ Å [22]. Thus, we concluded that the Li-depleted derivative has a composition $Li_{0.4}CoO_2$. For the NMC oxide, the refined unit cell parameter for the lithium-depleted phase are $a = 2.8182(8)$ and $c = 14.467(5)$ Å. The refined values of the unit cell parameters well agree with the data for the $Li_{0.2}Ni_{0.5}Mn_{0.3}Co_{0.2}O_2$ oxide with a reduced content of Li: $a = 2.8176$ and $c = 14.467$ Å [33]. Thus, we assumed the composition of the Li-depleted NMC phase as $Li_{0.2}$(Ni,Co,Mn)O_2.

For the minority phase constituent, $LiMn_2O_4$, the depleted Li content was assumed to be 0.75 Li atom/formula unit. This conclusion is based on the analysis of the voltage-discharge capacity curve (Fig. 4), where the plateau observed at 4.05 V is associated with this spinel phase. Based on the available reference data [40], within the used voltage window, when reaching 4.05 V, this phase is capable to be depleted by 0.25 Li atom/f.u only resulting in the formation of $Li_{0.75}Mn_2O_4$ at the end of the charge (see Fig. 5). The contribution of $LiMn_2O_4$ into the diffraction pattern is rather weak and because of that this phase was not included into the refinements.

Electrochemical delithiation of the saturated by Li layered oxides $LiCoO_2$ and Li(NMC)O_2 is accompanied by a deformation of their unit cells. A partial replacement of Co in $LiCoO_2$ by Mn and Ni to form Li(NMC)O_2 leads to a significant expansion of the unit cell (+4.5 vol %), with enlargement of both *a* and *c* taking place.

The changes taking place during the electrochemical delithiation of the cathode are manifested by the shift of the (003) peaks of both NMC and $LiCoO_2$ cathode phases towards the lower diffraction angles, indicating an expansion of their unit cells along [001].

A complete reversibility of the intercalation-deintercalation processes was observed for the layered oxides as the cathode electrode. The weight abundancies of the constituent phases in the fully charged and discharged battery obtained from Rietveld refinement are shown in Fig. 6 (see also Fig. S7). The refined abundancies of the cathode phases NMC: $LiCoO_2$ are slightly different for the charged and discharged battery being 47:53 for the fully charged state and 49:51 for the fully discharged state. However, this difference is considered as not significant accounting the accuracies of both EDS and multicomponent Rietveld refinements of the NPD data (around ± 3%).

2.4. In operando NPD study of the battery during charge and discharge

In situ NPD patterns were collected in a continuous acquisition mode over the course of 25 h, during which the battery was cycled at C/12.5 rates for both charge/discharge cycles. The data were concatenated into diffraction patterns every 5 min and these were integrated over 8 individual patterns. In total, 32 data sets were collected.

A 2D plot of the diffraction pattern observed in the region $21^\circ \leq 2\theta \leq 28^\circ$, showing the structural (see Fig. S8) changes in the anode during the discharge and charge, is presented in Fig. 7.

During the discharge, when Li^+ ions are extracted, the intensity of the (001) peak of LiC_6 rapidly decreases. The LiC_6 peak completely vanishes after 3.5 h of discharge. Then, the (002) peak of LiC_{12} appears and its intensity steadily increases as discharge proceeds. Next, we can see a gradual shifting of the (002) LiC_{12} peak towards the higher angles associated with a decrease of the *c* parameter for LiC_{12}. This shift indicates a continuous phase change witnessed by a step-by-step contraction of its unit cell associated with Li depletion. Such a behavior indicates the occurrence of a solid-solution phase, denoted hereafter as Li_xC_{12}, with composition

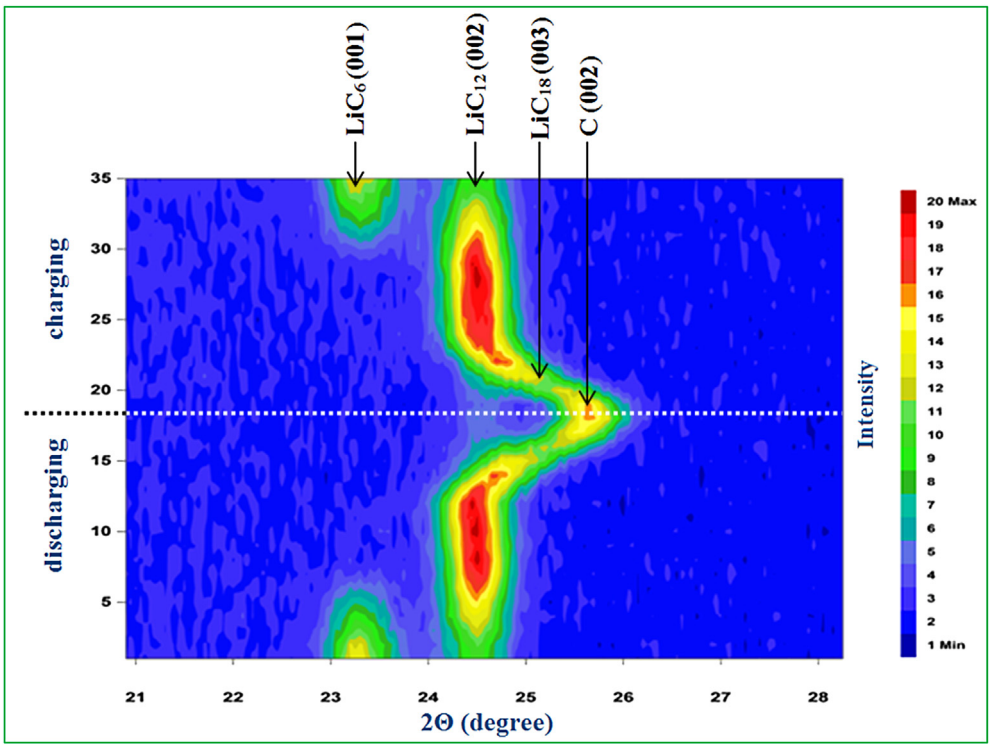

Fig. 6. 2D-plot of a selected area of the *in situ* ND pattern of anode during a discharge-charge cycle. The color scale (right axis) represents the diffraction peaks intensities (red: the highest intensity; blue – the lowest intensity). (For interpretation of the references to color in this figure legend, the reader is referred to the web version of this article.)

ranging from $x = 1$ (LiC_{12}) to $x = 2/3$ (LiC_{18}). Finally, the (002) peak from graphite appears after 10 h of discharge.

Gradual depletion of Li from Li_xC_{12} was witnessed by the appearance of the (003) peak (2θ ~24.9°) of LiC_{18} ($Li_{0.666}C_{12}$) at 90% of discharge (Fig. S9). This peak has been observed in a window 90–95% discharge. However, the refinements showed presence of some traces of LiC_{12} which still exist in the anode in parallel with LiC_{18} during the process of discharge. This indicates presence of kinetic limitations hindering a completeness of a transformation $LiC_{12} \rightarrow C$.

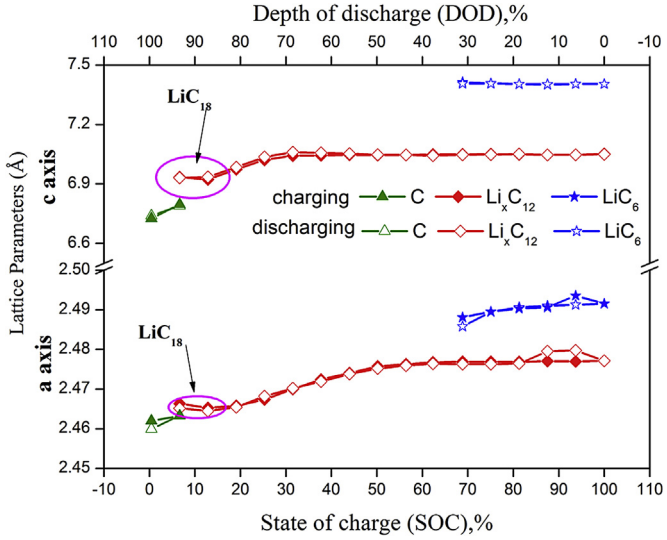

Fig. 7. Changes in the unit cell parameters (*a* and *c*) of the graphite anode during charge and discharge, derived from Rietveld refinements of the diffraction data. Both *a* and *c* of the lithiated graphite intercalates are normalized to the unit cell of graphite. The lattice parameters for the remaining at the end of discharge LiC_{12} (>95% DOD), being also present at the start of charge, are not shown here.

A broad peak at 2θ ~24–26° (Fig. S9) develops at the last stages of discharge (95% discharge), and corresponds to the overlapping reflections from LiC_{18} (003) and graphite (002). The peak shape is well described by assuming the presence of a mixture of LiC_{18} (38%) and graphite (62%). A successful Rietveld modeling (Fig. S10) of the shape of the peak confirms that, in the studied system, LiC_{18} is the intercalate with the lowest Li content formed. Any composition with a lower content than Li/C = 1:18 contains a mixture of LiC_{18} and graphite. The unit cell parameters of LiC_{18} (a = 4.289 (1) Å, c = 10.571(4) Å) well agree with the reference data [19] (a = 4.29 Å, 10.42 Å). For LiC_{18}, further to the (003), two resolved diffraction peaks were observed at higher diffraction angles, including (110) and (202), at 2θ = 40.86° and 88.57°, respectively.

Previously, both LiC_{18} ($Li_{0.33}C_6$) and LiC_{24} ($Li_{0.25}C_6$) were reported in the reference data as individual intercalation derivatives with the lowest content of Li [21,42]. The present study concludes that LiC_{18} rather than LiC_{24} is formed at the applied experimental conditions.

The LiC_{18} reflection disappears after 95% of charge. At the end of discharge (100% Depth of Discharge, DOD), the anode contains graphite and traces of LiC_{12}, which implies that the process of delithiation was not complete.

During the charge, the graphite first transforms into LiC_{18} and then the content of lithium in the Li_xC_{12} solid solution gradually increases until reaching a composition LiC_{12}. Then, after 10 h of the charge, the (001) peak of the LiC_6 phase appears manifesting an onset of transformation of LiC_{12} into the LiC_6.

A two-step lithiation intercalation process $C \rightarrow Li_xC_{12} \rightarrow LiC_6$ results in the formation of LiC_6 as the most Li-enriched product. Interestingly, LiC_6 starts to develop only after reaching 70% of the charging capacity. The coexistence of LiC_{12} and LiC_6 in the fully charged battery shows that the phase transformation of LiC_{12} into

LiC_6 has not been completed, as the anode has a larger charge capacity as compared to the cathode.

The changes in the intensities of the (002) LiC_{12} and (001) LiC_6 Bragg reflections (Fig. S11) manifesting the changes in their abundances during the charge of the battery, illustrate the kinetics of the transformations in the two phase region $LiC_{12} + LiC_6$ at the applied charge rate of C/12.5. An intensity reduction for the graphite Bragg peak (002) clearly shows the kinetics of the staged Li insertion into the graphite. For the complete lithiation of graphite into LiC_6, the *a* axis slightly increases ($\Delta a/a = 1.2\%$) while an expansion of the interlayer distances along [001] is much more significant ($\Delta c/c = 10.1\%$). Thus, in total, upon charging, formation of LiC_6 leads to a volume expansion of ~12.7%.

On charging, intercalation of Li into graphite to form LiC_{18} results in a discrete increase of the *a* and *c* unit cell parameters (Fig. 7). Further Li intercalation into LiC_{18} results in the formation of Li_xC_{12} ($x = 2/3–1$) solid solution and gives a gradual increase of both *a*- and *c*- unit cell parameters. This increase is related to the growing amount of Li in the lattice and follows the state-of-charge of the battery. After reaching 70% of charge, the unit cell parameters of LiC_{12} remain constant. While discharging, the changes in both *a* and *c* unit cell parameters follow a reverse pathway, - until the formation of graphite takes place.

For the cathode materials, a common feature for both layered oxides is the expansion of the unit cells along [001] taking place during the charging/delithiation. The shifts of the (003) peak of the layered oxides as related to the different states of charge are shown in Fig. 8. These peaks shift towards the lower angles while charging, indicating the expansion of the unit cells along [001]. However, a much more significant expansion along [001] takes place during a transformation $LiCoO_2 \rightarrow Li_{0.4}CoO_2$ ($\Delta c/c = 2.7\%$). The expansion is, however, marginal for $Li_{1-x}(NMC)O_2$ ($\Delta c/c = 0.40\%$).

A contraction of the unit cells takes place in the basal plane for both $Li_{0.2}(NMC)O_2$ and for $Li_{0.4}CoO_2$; the changes of $\Delta a/a$ are also uneven and are much more pronounced for the NMC oxide (−0.9%) as compared to $Li_{0.4}CoO_2$ (−0.2%).

The lattice dilation of NMC is similar to the observations of [27], where the reduction of the cell volume during the charging was also observed. In the case of $LiCoO_2$, an expansion of the unit cell by 2.2% upon cell charge is in agreement with [43].

Thus, similar lattice behavior in $LiCoO_2$ and NMC cathode results in opposite unit cell volume changes, - an expansion of the unit cell for $Li_{0.4}CoO_2$ and its contraction for $Li_{0.2}(NMC)O_2$. Such changes can be explained by the higher valence state of Mn (+4) in $Li_{1-x}(MNC)O_2$ and the possibility to extract more Li by oxidizing Ni^{2+} to Ni^{4+}, as compared to the (+3) valence configuration of Co in $Li_{1-x}CoO_2$. The values of the unit cell parameters and volumes of the unit cells at various stages of charge are listed in Table 4.

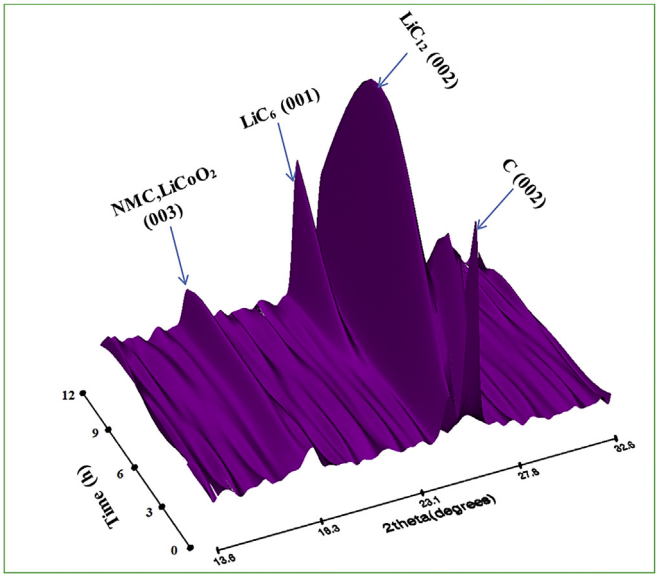

Fig. 8. 3D plot of the *in situ* NPD pattern during the charging of the battery. A parallel development of the (003) Bragg peak of the $LiCoO_2$ and $Li(Ni,Mn,Co)O_2$, together with graphite (002), LiC_{12} (002) and LiC_6 (001) peaks is shown.

3. Conclusions

A commercial Li ion battery was characterized *in operando* during its charge and discharge using neutron powder diffraction. These studies revealed the mechanism of the transformations in the graphite anode and in the multiphase cathode, which contained $Li(Ni,Mn,Co)O_2$ and $LiCoO_2$ as the major phase constituents in the presence of spinel $LiMn_2O_4$. The processes taking place in this multiphase commercial cathode were studied for the first time.

Exactly inverted pathways of transformation were identified for the graphite anode during charging and discharging, with the intermediate formation of a solid solution phase Li_xC_{12} between the LiC_{12} and LiC_{18} intercalates. During the charge/discharge, two discrete phase transformations C ↔ LiC_{18} and LiC_{12} ↔ LiC_6 take place in the graphite anode. The most Li-saturated stable graphite intercalate phase LiC_6 starts to form only after reaching about 75% of charge, causing a decrease in the amount of the LiC_{12} intercalate. At the fully charged state, only 50% of the LiC_{12} converts to LiC_6. This is attributed to the chosen anode capacity being larger than that of the cathode in the commercial battery.

The discharge voltage profiles show different plateaus, which are associated with the redox potentials of the three cathode phases. A more significant discharge of the NMC oxide than for the $LiCoO_2$ is observed at the same final charge voltage of 4.2 V at a full charge state of the battery, leading to the formation of $Li_{0.4}CoO_2$ and $Li_{0.2}Ni_{0.5}Mn_{0.3}Co_{0.2}O_2$.

We observed the expansion and contraction of the unit cells of the $LiCoO_2$ and NMC (532) oxide during discharge of the battery, showing that it is influenced by the chemistry of the transition metal component.

The most significant change during the delithiation was observed for $LiCoO_2$, where the cell volume increases by 2.2%, which may be caused by the repulsion between the negatively charged CoO_2 layers during the depletion of the lattice by Li, while the NMC cathode demonstrates a volume shrinking of ~1.4%, showing that the repulsion between the TMO_2 layers is less

Table 4
Comparison of lattice parameters of the layered oxides at different state of charge.

x in $Li_xM^*O_2$/Phase	$Li_x(Ni,Mn,Co)O_2$	Li_xCoO_2
1	$a = 2.844(1)$ $c = 14.41(1)$ $V = 100.94$ Å^3	$a = 2.817(3)$ $c = 14.060(2)$ Å $V = 96.625$ Å^3
0.84	$a = 2.8276(1)$ Å $c = 14.494(1)$ Å; $V = 100.357(8)$ Å^3	–
0.75	–	$a = 2.8120(1)$ Å $c = 14.226(1)$ Å $V = 97.419(5)$ Å^3
0.4	–	$a = 2.8100(3)$ $c = 14.445(3)$ Å $V = 98.778$ Å^3
0.2	$a = 2.8182(8)$ $c = 14.467(5)$ Å $V = 99.507$ Å^3	–

* M-(Ni,Mn,Co), Co.

significant in $Li_{1-x}(Ni,Mn,Co)O_2$. The lattice dilation in NMC can be explained in terms of the charge compensations in the transition metal ions, i.e, the valence change of the transition metals changes upon charge-discharge by Li. The NMC cathode contains Mn^{4+}, Co^{3+} and Ni^{2+} at the fully lithiated state. When the battery is close to completely charged (i.e, Li ions are nearly fully removed from the cathode), the valence of Ni ions changes to Ni^{4+} and the ionic radius decreases. As a result of this, the edge sharing NiO_6 octahedra shrink along in the basal plane and the NiO_6 slabs becomes positively charged and repel each other along the c axis. Thus, the lattice expanded along the *c* axis. Even though the volumetric effects are uneven in size for the two main cathode phases, most importantly, these two oxides showed complete lattice reversibility during the intercalation/deintercalation of Li atoms.

Studies of the battery discharge performance has shown that the highest battery efficiency was reached at 45 °C when, even at the highest discharge current densities of 2 C, the battery delivered 91% of the stored electrochemical capacity. In contrast, at the lowest testing temperature (5 °C), the battery significantly reduces the cell capacity at the discharge current density of 2 C. Interestingly, even a small temperature increase results in a change of the mechanism of the discharge processes, leading to a better battery performance.

This work proves that *in situ* neutron diffraction studies of a commercial Li ion battery during its charge and discharge generate new insights into the complex mechanism and kinetics of structural changes in the anode and cathode materials during their operation. This work will allow further optimization of the battery performance through appropriate selection of the chemistry of both electrodes and by suitable engineering of the battery setup.

Acknowledgements

This work was supported by Research Council of Norway and the European Spallation Source (Project 234246 “HIGH POWER BATTERIES PROBED BY NEUTRON SCATTERING”) .

The work is partly based on the experiments performed at the Swiss spallation neutron source SINQ, Paul Scherrer Institute, Villigen, Switzerland. We sincerely appreciate help from HRTP instrument responsible scientist Dr. D. Sheptyakov during the performed experiments.

We are grateful to the marketing department of Great Power Battery Co., Ltd. (H.K./China) for sharing an overview of the technology development in the company, for providing the catalogue of the commercial products and for the battery cells utilized in the present study.

Appendix A. Supplementary data

Supplementary data related to this article can be found at http://dx.doi.org/10.1016/j.jpowsour.2016.06.105.

References

[1] N. Nitta, F. Wu, J.T. Lee, G. Yushin, Mater Today 18 (2015) 252–264.
[2] S.M. Rezvanizaniani, Z. Liu, Y. Chen, J. Lee, J. Power Sources 256 (2014) 110–124.
[3] A. Barré, B. Deguilhem, S. Grolleau, M. Gérard, F. Suard, D. Riu, J. Power Sources 241 (2013) 680–689.
[4] B. Scrosati, J. Garche, J. Power Sources 195 (2010) 2419–2430.
[5] W.-J. Zhang, J. Power Sources 196 (2011) 877–885.
[6] D. Doughty, E.P. Roth, Electrochem Soc. Interface 21 (2012) 37–44.
[7] M. Ma, N.A. Chernova, B.H. Toby, P.Y. Zavalij, M.S. Whittingham, J. Power Sources 165 (2007) 517–534.
[8] P. Rozier, J.M. Tarascon, J. Electrochem. Soc. 162 (2015) A2490–A2499.
[9] K. Min, K. Kim, C. Jung, S.-W. Seo, Y.Y. Song, H.S. Lee, J. Shin, E. Cho, J. Power Sources 315 (2016) 111–119.
[10] G.W. Ling, X.P. Zhu, Y.B. He, Q.S. Song, B.H. Li, Y.J. Li, Q.H. Yang, Z.Y. Tang, Int. J. Electrochem. Sci. 7 (2012) 2455–2467.
[11] M.M. Thackeray, S.-H. Kang, C.S. Johnson, J.T. Vaughey, R. Benedek, S.A. Hackney, J. Mater, Chem. 17 (2007) 3112.
[12] X. Feng, Z. Yang, D. Tang, Q. Kong, L. Gu, Z. Wang, L. Chen, Phys. Chem. Chem. Phys. 17 (2015) 1257–1264.
[13] A.M. Kannan, A. Manthiram, Electrochem. Solid State Lett. 5 (2002) A167.
[14] E.J. Berg, C. Villevieille, D. Streich, S. Trabesinger, P. Novák, J. Mater. Chem. A 162 (2015) A2468–A2475.
[15] Y. Qi, S.J. Harris, J. Electrochem. Soc. 157 (2010) A741.
[16] P.P.R.M.L. Harks, F.M. Mulder, P.H.L. Notten, J. Power Sources 288 (2015) 92–105.
[17] N. Sharma, W.K. Pang, Z. Guo, V.K. Peterson, ChemSusChem 8 (2015) 2826–2853.
[18] V. Zinth, C. von Lüders, M. Hofmann, J. Hattendorff, I. Buchberger, S. Erhard, J. Rebelo-Kornmeier, A. Jossen, R. Gilles, J. Power Sources 271 (2014) 152–159.
[19] W.K. Pang, M. Alam, V.K. Peterson, N. Sharma, J. Mater. Res. 30 (2015) 373–380.
[20] O. Dolotko, A. Senyshyn, M.J. Mühlbauer, K. Nikolowski, H. Ehrenberg, J. Power Sources 255 (2014) 197–203.
[21] A. Senyshyn, O. Dolotko, M.J. Muhlbauer, K. Nikolowski, H. Fuess, H. Ehrenberg, J. Electrochem. Soc. 160 (2013) A3198–A3205.
[22] O. Dolotko, A. Senyshyn, M.J. Muhlbauer, K. Nikolowski, F. Scheiba, H. Ehrenberg, J. Electrochem. Soc. 159 (2012) A2082–A2088.
[23] N. Sharma, V.K. Peterson, Electrochim. Acta 101 (2013) 79–85.
[24] A. Senyshyn, M.J. Mühlbauer, O. Dolotko, H. Ehrenberg, J. Power Sources 282 (2015) 235–240.
[25] A. Senyshyn, M.J. Mühlbauer, K. Nikolowski, T. Pirling, H. Ehrenberg, J. Power Sources 203 (2012) 126–129.
[26] N. Sharma, V.K. Peterson, J. Power Sources 244 (2013) 695–701.
[27] X.L. Wang, K. An, L. Cai, Z. Feng, S.E. Nagler, C. Daniel, K.J. Rhodes, A.D. Stoica, H.D. Skorpenske, C. Liang, W. Zhang, J. Kim, Y. Qi, S.J. Harris, Sci. Rep. 2 (747) (2012) 1–7.
[28] M. Bianchini, J.B. Leriche, J.-L. Laborier, L. Gendrin, E. Suard, L. Croguennec, C. Masquelier, J. Electrochem. Soc. 160 (2013) A2176–A2183.
[29] P. Fischer, G. Frey, M. Koch, M. Könnecke, V. Pomjakushin, J. Schefer, R. Thut, N. Schlumpf, R. Bürge, U. Greuter, S. Bondt, E. Berruyer, Phys. B 276–278 (2000) 146–147.
[30] B.H. Toby, J. Appl. Crystallogr. 34 (2001) 210–213.
[31] A.C. Larson, R.B.V. Dreele, Los Alamos National Laboratory Report LAUR, 2004, 86–748.
[32] Y. Takahashi, N. Kijima, K. Dokko, M. Nishizawa, I. Uchida, J. Akimoto, J. Solid State Chem. 180 (2007) 313–321.
[33] S. Lee, D. Jang, J. Yoon, Y.H. Cho, Y.S. Lee, D.H. Kim, W.S. Kim, W.S. Yoon, J. Electrochem. Sci. Technol. 3 (2012) 29–34.
[34] H.M. Wu, J.P. Tu, X.T. Chen, Y. Li, X.B. Zhao, G.S. Cao, J. Electroanal. Chem. 586 (2006) 180–183.
[35] Y. Imai, A. Watanabe, J. Alloys Compd. 439 (2007) 258–267.
[36] M.C. Smart, B.V. Ratnakumar, J. Electrochem. Soc. 158 (2011) A379–A389.
[37] Y. Ji, Y. Zhang, C.Y. Wang, J. Electrochem. Soc. 160 (2013) A636–A649.
[38] S. Yang, X. Wang, X. Yang, Z. Liu, Q. Wei, H. Shu, Int. J. Electrochem. Sci. 2012 (2012) 1–9.
[39] T. Wei, R. Zeng, Y. Sun, Y. Huang, K. Huang, Chem. Commun. 50 (2014) 1962–1964.
[40] X. Zhang, H. Zheng, V. Battaglia, R.L. Axelbaum, J. Power Sources 196 (2011) 3640–3645.
[41] H. Ben Yahia, M. Shikano, H. Kobayashi, Chem. Mater 25 (2013) 3687–3701.
[42] D. Billaud, F.X. Henry, M. Lelaurain, P. Willmann, J. Phys. Chem. Solids 57 (1996) 775–781.
[43] N. Sharma, V.K. Peterson, J. Solid State Electrochem 16 (2011) 1849–1856.

SUPPLEMENTARY INFORMATION TO THE MANUSCRIPT

In Operando Neutron diffraction study of a Commercial Graphite / (Ni, Mn, Co) Oxide-Based Multi-component Lithium Ion Battery

N. S. Nazer[1, 2], V.A. Yartys[1, 2*], T. Azib[3], M. Latroche[3], F. Cuevas[3], S. Forseth[4], P.J.S. Vie[1], R.V. Denys[1], M.S. Sørby[1], B.C. Hauback[1], L. Arnberg[2] and P.F.Henry[5]

(1) Institute for Energy Technology, Kjeller, Norway; (2) NTNU, Trondheim, Norway;
(3) Université Paris Est, ICMPE (UMR7182), CNRS, UPEC, F-94320 Thiais, France;
(4) FFI, Norway; (5) European Spallation Source ERIC, Sweden

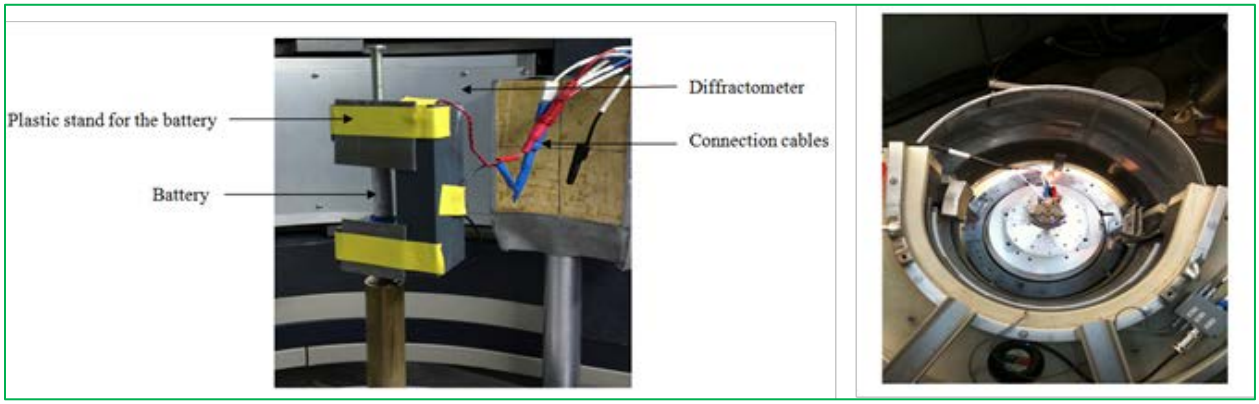

Figure S1. Experimental setup for the *in situ* diffraction study of the battery cell (left) with a top view of the HRPT diffractometer (SINQ, PSI) shown in the right part.

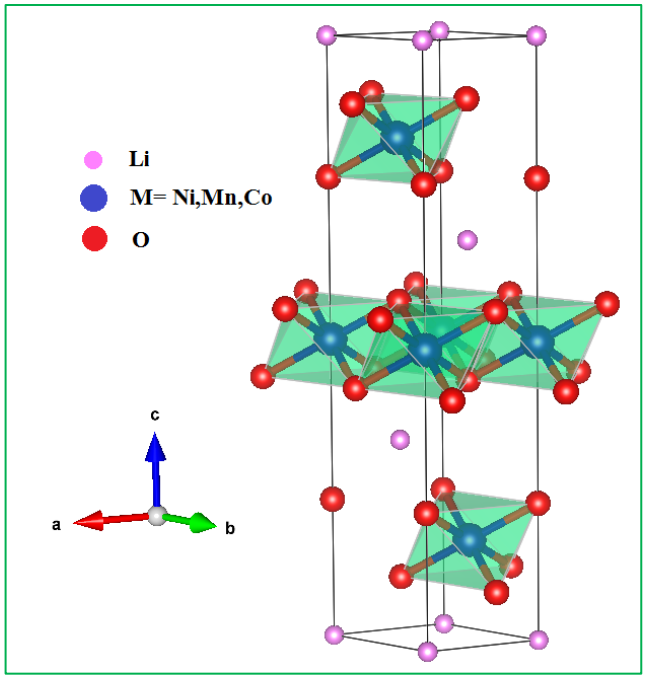

Figure S2. Schematic view of the layered oxide - $Li(Ni,Mn,Co)O_2$ (space group $R\bar{3}m$). The MO_6 octahedra are shown. For the isostructural $LiCoO_2$, with Li depletion, the repulsion between adjacent CoO_2^- layers increases resulting in expansion of the unit cell along the *c* axis.

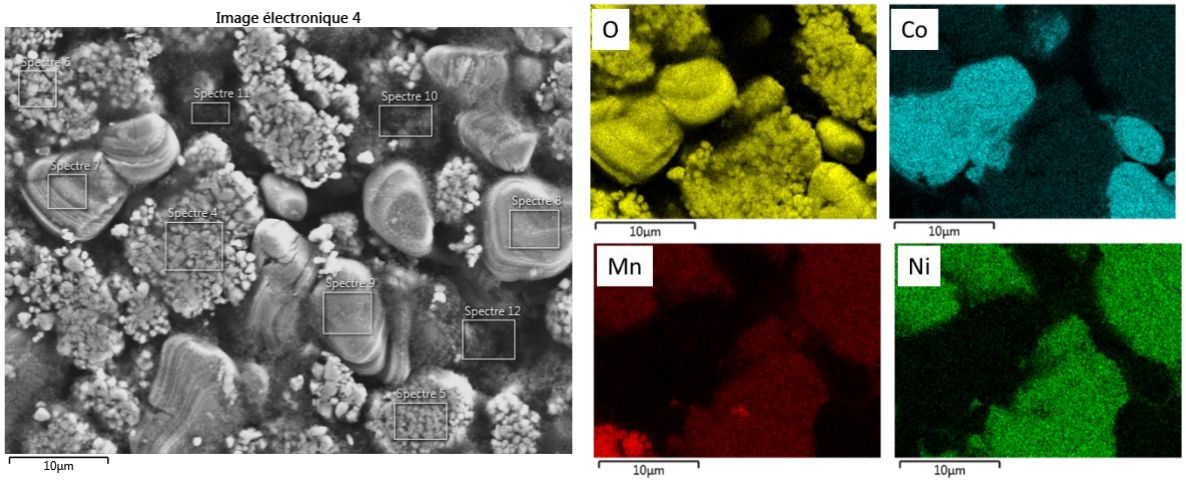

Figure S3: SEM image and EDX elemental map distribution for the active material deposited on the positive electrode.

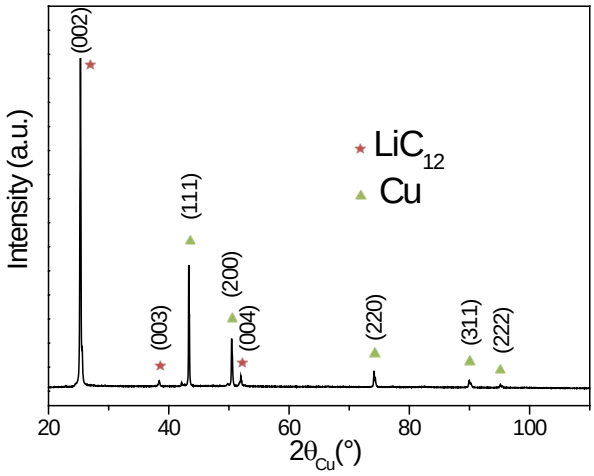

Figure S4. XRD pattern of the graphite anode showing that in the as-supplied battery the anode material is in the form of a partially lithiated graphite LiC_{12}.

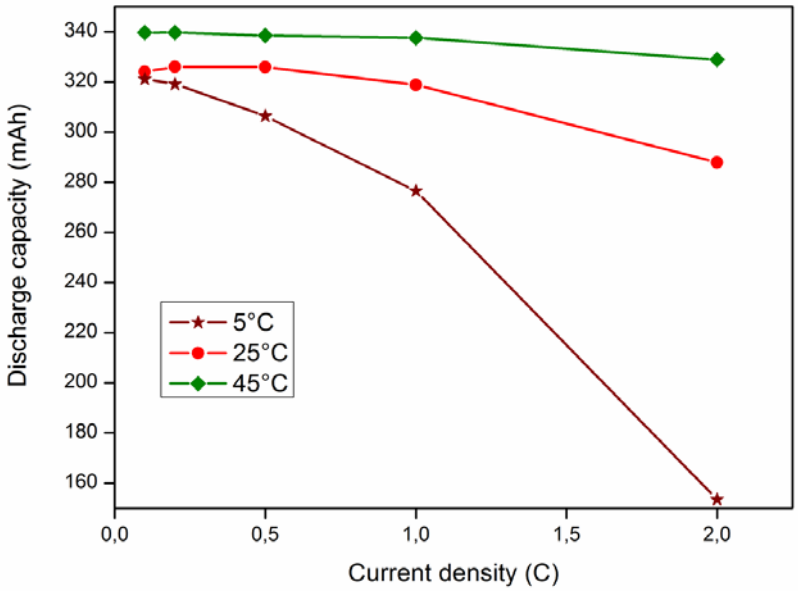

Figure S5. Discharge capacity as related to the applied discharge regime at 5°C, 25°C and 45°C in the ICR10440 Li-ion battery.

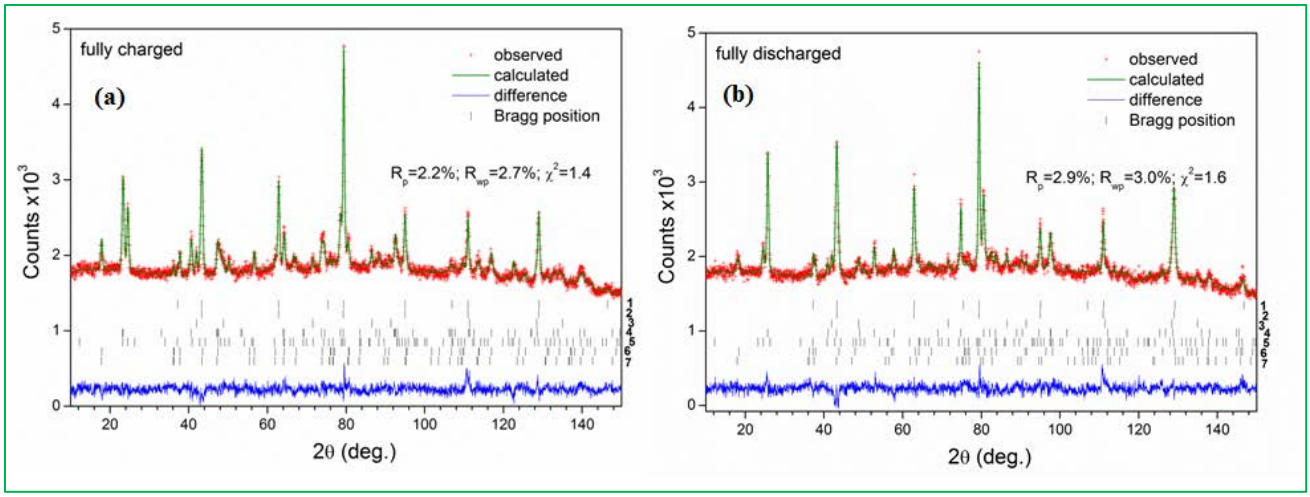

Figure S6. Neutron diffraction patterns for the fully charged (a) and discharged (b) battery along with the results of the Rietveld refinements. Phase constituents, from bottom to top:

(a) $Li_{0.2}(NMC)O_2$, $Li_{0.4}CoO_2$, LiC_{12}, LiC_6, Cu, Fe, Al.
(b) $Li(NMC)O_2$, $LiCoO_2$, LiC_{12}, C, Cu, Fe, Al.
R_{wp}=2.7%, R_p=2.2%, ; χ^2=1.4 and R_{wp}=3.0%, R_p=2.9% ; χ^2=1.6, respectively, with 13 refined variables for the fully charged battery (a) and discharged battery (b).

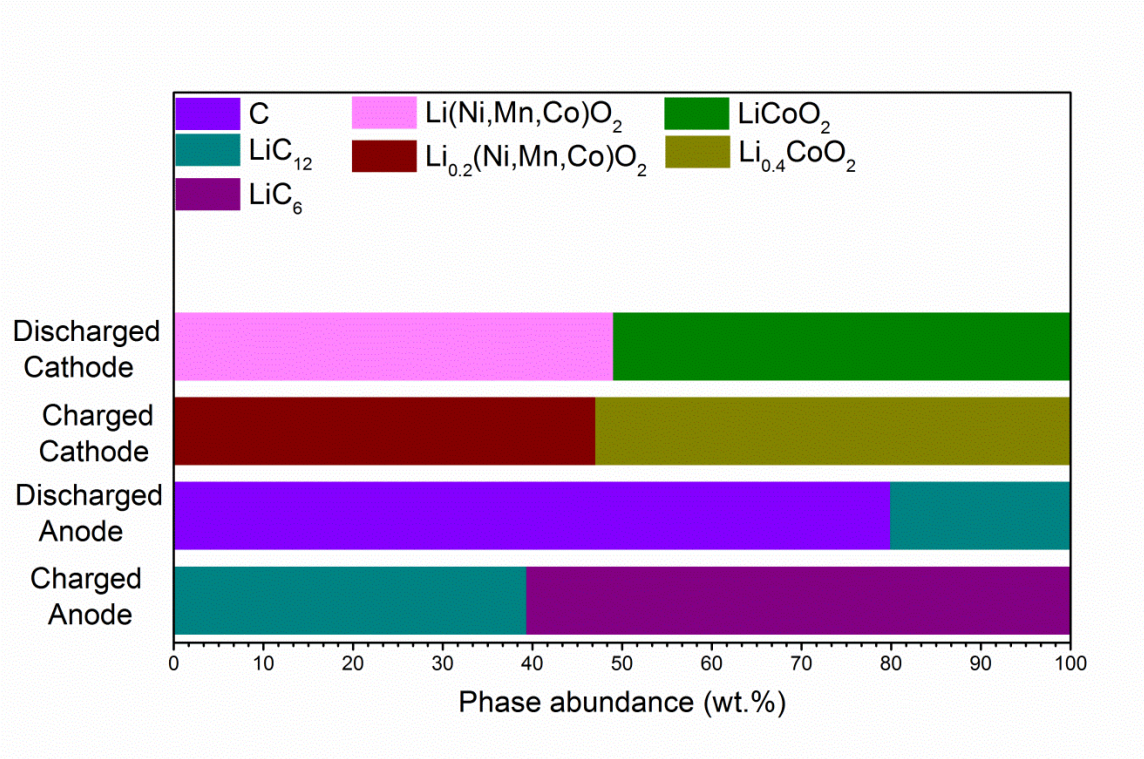

Figure S7. Normalized phase abundances obtained from the Rietveld refinements of NPD data.

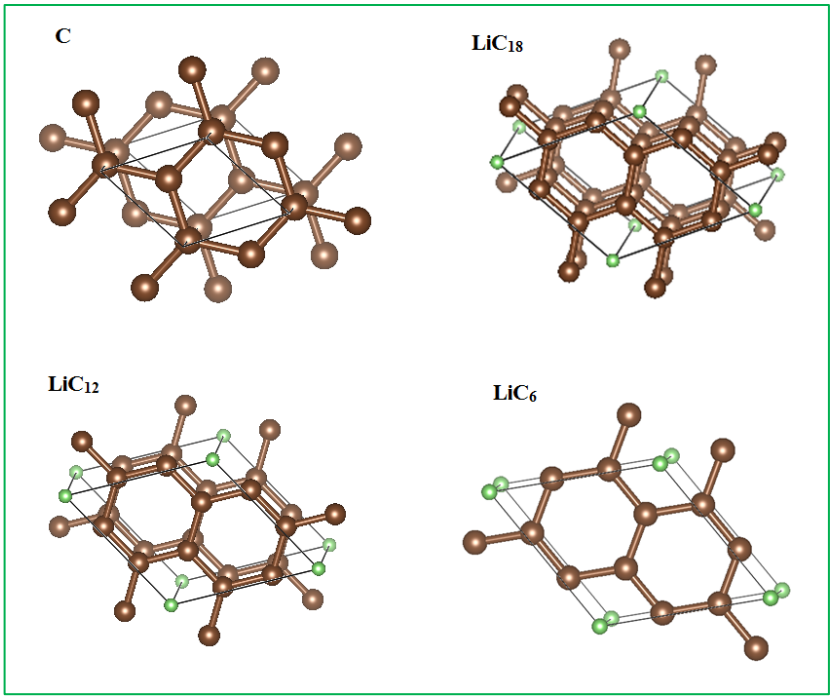

Figure S8. Structure of graphite and lithium intercalated graphite derivatives. The brown atoms are C and the green atoms are Li. Li is intercalated into every third layer of graphene sheets in LiC_{18} (stage 1), every second layer in LiC_{12} (stage 2), and finally it resides in every layer in LiC_6 (stage 3).

Relationship between the unit cells of graphite and lithiated graphite intercalates.

LiC_6	LiC_{12}	LiC_{18}
$a=a_{graphite}\times\sqrt{3}$ $c=c_{graphite}/2$	$a=a_{graphite}\times\sqrt{3}$ $c=c_{graphite}$	$a=a_{graphite}\times\sqrt{3}$ $c=c_{graphite}\times 3/2$

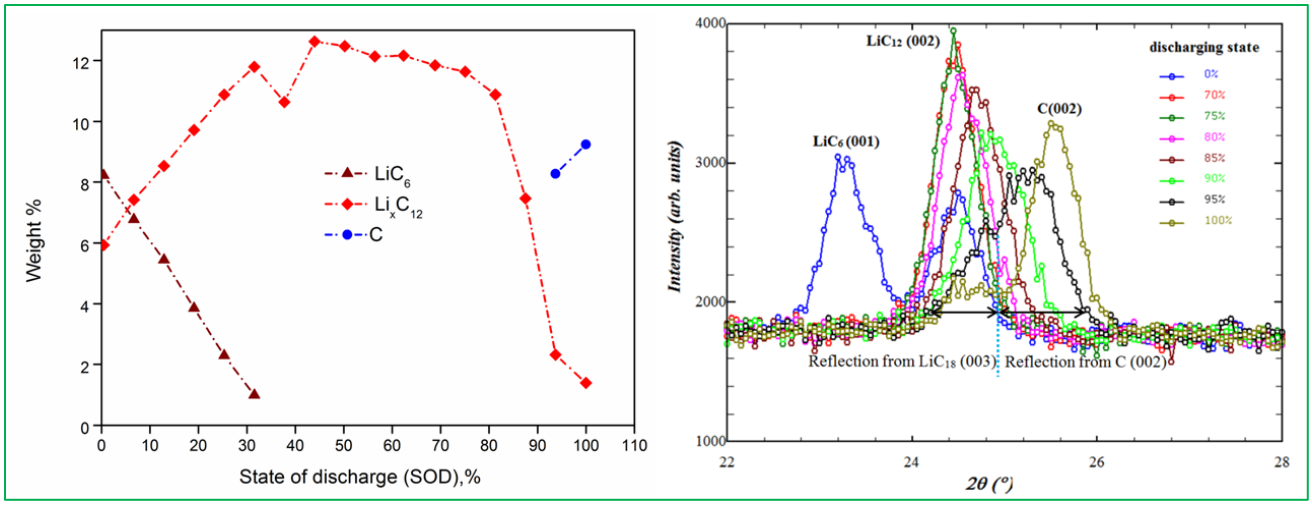

a **b**

Figure S9. Intensity evolution of the (00*l*) Bragg reflections for the lithiated graphite intercalates during discharging (a) and development of the C (002) peak at the end of discharge (b).

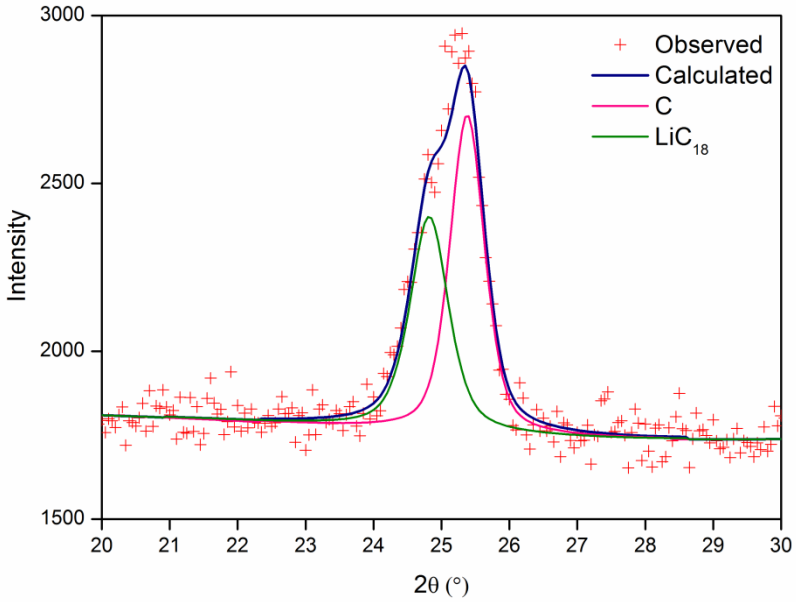

Figure S10. Rietveld refinement shows the deconvolution of the NPD peak at 2θ ~24 to 26° into two peaks coming from graphite and LiC_{18}. The refined weight ratio C: LiC_{18} is = 60:40. Battery at 95% SOD.

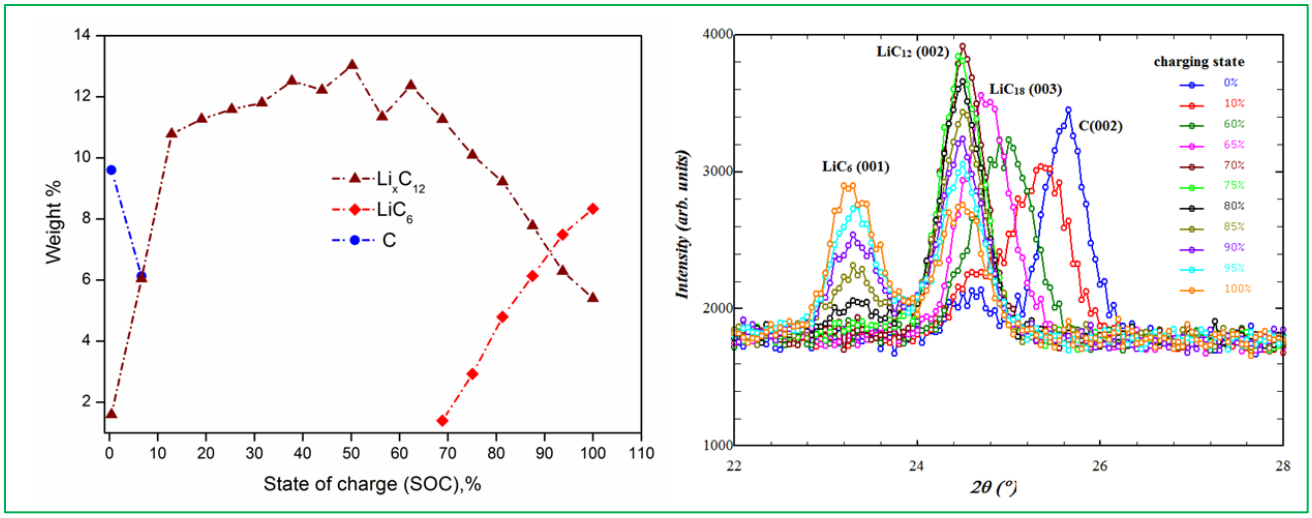

Figure S11. Intensity evolution of the (00*l*) Bragg reflections for graphite and lithiated graphite during charging of the battery.